Detecting Multiplanetary Systems with Gravitational Microlensing and the Roman Space Telescope

Hossein Fatheddin and Sedighe Sajadian
Department of Physics, Isfahan University of Technology, Isfahan 84156-83111, Iran

Abstract

It is plausible that most of the Stars in the Milky Way Galaxy, like the Sun, consist of planetary systems, instead of a single planet. Out of the estimately discovered 3980 planet-hosting stars, about 860 of them are known to be multiplanetary systems (as of 2023 June). Gravitational microlensing, which is the magnification in the light of a source star, due to a single or several lenses, has proven to be one of the most useful astrophysical phenomena with many applications. Until now, many extrasolar planets (exoplanets) have been discovered through binary microlensing, where the lens system consists of a star with one planet. In this paper, we discuss and explore the detection of multiplanetary systems that host two exoplanets via microlensing. This is done through the analysis and modeling of possible triple-lens configurations (one star and two planets) of a microlensing event. Furthermore, we examine different magnifications and caustic areas of the second planet, by comparing the magnification maps of triple and binary models in different settings. We also discuss the possibility of detecting the corresponding light curves of such planetary systems with the future implementation of the Nancy Grace Roman (Roman) Space Telescope and its Galactic Time Domain survey.

Unified Astronomy Thesaurus concepts: Exoplanet detection methods (489); Gravitational microlensing (672); Gravitational microlensing exoplanet detection (2147)

Supporting material: animations

1. Introduction

The first discovery of a planet around a solar-type star came in 1995, when a Jovian-mass planet orbiting the star 51 Pegasi was detected from observations of periodic variations in the radial velocity of the star (Mayor & Queloz 1995). Since then, the exoplanet research has evolved dramatically, involving a broad range of observational and theoretical effort.

Due to the lack of proper observational instruments and the difficulties of directly imaging exoplanets, most of these objects are detected indirectly (Fischer et al. 2014) mostly with the following methods (see Wright & Gaudi 2013): Astrometric and Doppler Shift measurements (which are based on the perturbations of the radial velocity or proper motion of the host star), Timing (when a planet changes the priodicity in the brightness of a variable star), Transits (which is based on the change in the photometric light curve of a star, caused by a passing planet), and Microlensing.

The Kepler/K2 space missions for detecting exoplanets with the transit method have shown that it is quite common for a star to host multiple planets and many multiplanetary systems have been discovered this way (Livingston et al. 2019; Maltagliati 2019).

Since our discussion of detecting multiplanetary systems is mainly based on the microlensing method, we will review some of its principles and foundations, in the following passages.

Since their first discovery in 1993 (Alcock et al. 1993; Aubourg et al. 1993; Udalski et al. 1993), gravitational microlensing events have provided astronomers and astrophysicists with a powerful tool for studying various objects,

ranging from exoplanets to black holes. These events act as natural telescopes that can magnify and lead to the detection of some of the darkest objects in our universe, such as exoplanets orbiting the lens objects (Mao & Paczynski 1991; Gould & Loeb 1992; Bennett & Rhie 1996; Bennett 2008), Massive Astrophysical Compact Halo Objects (Alcock et al. 1997, 2000), Free Floating Planets (Sumi 2014; Sajadian 2021a), and even Isolated Black Holes in the Galactic disk (Sahu et al. 2022; Sajadian & Sahu 2023).

The properties of microlensing events due to single and binary lenses have been studied in great details (see Liebes 1964; Refsdal 1964, 1966; Schneider & Weiss 1986). Currently, most of the exoplanets that are discovered via microlensing, belong to the category of binary events where a source star passes from behind two lenses; one star with its companion planet. The only change from the simple case of a single lens is that the deflection angle, which is caused by the gravitational field of the lens objects (Dyson et al. 1920), consists of the sum of two point lenses:

$$\alpha(\boldsymbol{x}) = \frac{4G}{c^2}\left(\frac{m_1(\boldsymbol{x}-\boldsymbol{x}_1)}{(\boldsymbol{x}-\boldsymbol{x}_1)^2} + \frac{m_2(\boldsymbol{x}-\boldsymbol{x}_2)}{(\boldsymbol{x}-\boldsymbol{x}_2)^2}\right), \qquad (1)$$

where m_1, m_2 are the masses of the two lenses and $\boldsymbol{x}_1, \boldsymbol{x}_2$ are their positions. Here, we assume two lens objects are in the same distances from the observer.

The binary lens equation, in its complex notation, was derived by Witt (1990):

$$\zeta = z + \frac{\mu_1}{\bar{z}_1 - \bar{z}} + \frac{\mu_2}{\bar{z}_2 - \bar{z}}, \qquad (2)$$

where, $\mu_1 = m_1/(m_1+m_2)$, $\mu_2 = m_2/(m_1+m_2)$, z_1 and z_2 are the positions of the lenses, $\zeta = \xi + i\eta$ and $z = x + iy$ are the source and the image positions projected on the lens plane and

normalized to the Einstein radius (the radius of the images ring at the complete alignment). $\bar{z}$ indicates the complex conjugate of z. By doing some calculations (Witt & Mao 1995), the lens equation (Equation (2)) becomes a lengthy fifth order polynomial in z, which requires numerical solutions in order to trace the position of the images (Fatheddin & Sajadian 2022).

The binary microlensing method for detecting exoplanets relies on the existence of one planet in the lens system, but it is rare for a star to have only one planet. The complicated degeneracies, lack of fast and accurate models and lack of observational data, might be some of the causes for not detecting as many triple microlensing events as the binary ones (we discuss and review the probabilities of triple-lens events in more details at the end of Section 2.).

The first observation of triple-lens gravitational microlensing was done in 2006, when a gas giant was detected orbiting a stellar binary system (Bennett et al. 2020). The first triple-lens system consisting of one star and two planets, was detected in 2008 (Gaudi et al. 2008), when a Jupiter/Saturn planetary system Analog was discovered. Since then, a few other triple-lens systems, similar to these events, have been observed.

There are many lensing and microlensing projects that produce TBytes of data i.e., the Optical Gravitational Lensing Experiment (Udalski et al. 2015), the Microlensing Observations in Astrophysics (Sako et al. 2008) microlensing group, and the Korea Microlensing Telescope Network (Kim et al. 2016). The future implementation of ground and Space based surveys, like the Nancy Grace Roman Space Telescope (Roman) telescope (Penny et al. 2019) will produce even more data for triple-lens events.

In this paper, after discussing the properties of triple-lens systems in Section 2, we will analyze and study the properties of magnification maps of these systems in Section 3. In Section 4, we investigate the possibility of detecting the light curves of multiplanetary systems with the Roman space telescope. Finally, in the last section, we discuss and summarize the results.

2. Microlensing from Triple-lens Systems

In this section we are going to review some characteristics of microlensing due to a triple-lens system and its lens equation so that we can analyze the features and detection of multiplanetary systems in the next sections. The existence of a third lens object can cause several degeneracies in the lens equation, we review some of these degeneracies in Section 2.2. Since, most of the exoplanets that are detected with microlensing, belong to the category of binary lenses, we review some of the probabilistic comparisons between these events and events with triple lenses in the last part of this section.

2.1. Parameters of a Triple Lens System

When a source passes from behind three lenses, the only change from a binary lens situation (Equation (1)) is that the deflection angle now consists of the sum of three point lenses:

$$\alpha(\boldsymbol{x}) = \frac{4G}{c^2}\left(\frac{m_1(\boldsymbol{x}-\boldsymbol{x}_1)}{(\boldsymbol{x}-\boldsymbol{x}_1)^2} + \frac{m_2(\boldsymbol{x}-\boldsymbol{x}_2)}{(\boldsymbol{x}-\boldsymbol{x}_2)^2} + \frac{m_3(\boldsymbol{x}-\boldsymbol{x}_3)}{(\boldsymbol{x}-\boldsymbol{x}_3)^2}\right),$$
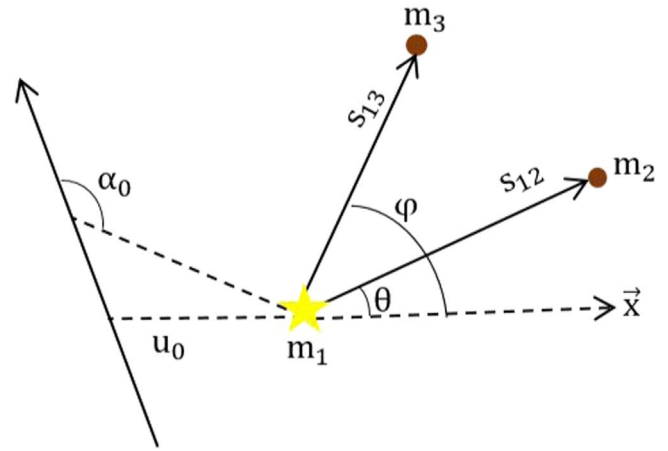(3)

Figure 1. Parameters of a Triple Lens system. The three lenses are labeled as m_1, m_2, m_3 (where m_1 is the host star and m_2 and m_3 are the planets). The trajectory of the source is also illustrated. The coordinate system is centered on the host star.

where m_1, m_2, m_3 are the masses of the three lenses, and $\boldsymbol{x}_1, \boldsymbol{x}_2, \boldsymbol{x}_3$ are their positions.

In gravitational lensing formalism, the Einstein radius, θ_E, which is the angular radius of the images ring at the time of complete alignment, is defined as:

$$\theta_E = \sqrt{\frac{4\,G\,M_l}{c^2}\frac{D_{ls}}{D_l\,D_s}},$$
(4)

where M_l is the lens mass, $D_{ls} = D_s - D_l$, D_l and D_s are the lens and source distance from the observer.

In a triple-lens scenario, we use the following parameters to analyze or model an event (Figure 1):

1. The mass ratios $q_{21} = m_2/m_1$ and $q_{31} = m_3/m_1$.
2. The triple separations s_{21} and s_{31} (projected on the lens plane and in units of the Einstein radius for the total masses; $M_l = m_1 + m_2 + m_3$).
3. The angle ϕ from the s_{12}-axis to the s_{13}-axis counterclockwise and the angle θ from the x-axis of the chosen coordinate system to the s_{12}-axis measured counterclockwise (also in the Einstein Radius).
4. Radius of the source ρ_* (also projected in the lens plane and in the Einstein Radius).
5. The impact parameter u_0.
6. The angle α_0 from the s_{12}-axis to the source trajectory counterclockwise.
7. Time of the closest approach t_0 and the Einstein crossing time t_E.

Changing any of these parameters allows for a very large variety of triple-lens light curves and makes triple lenses more complicated than binary ones, which were briefly reviewed in the introduction.

The triple-lens equation for a triple-lens system can be derived easily as (similar to Equation (2)):

$$\zeta = z + \frac{\mu_1}{\bar{z}_1 - \bar{z}} + \frac{\mu_2}{\bar{z}_2 - \bar{z}} + \frac{\mu_3}{\bar{z}_3 - \bar{z}},$$
(5)

where $\mu_i = m_i/M_l$, z_1, z_2, and z_3 are the positions of the lenses projected on the lens planet normalized to the Einstein radius, $\zeta = \xi + i\eta$ and $z = x + iy$ are the source and the image positions and $\bar{z}$ indicates the complex conjugate of z.

According to Rhie (2002), a polynomial form for this equation can be derived by choosing a coordinate system in a way that the position of a mass m_1, z_1, and the center of mass of the other two masses, defined as z_4, make the lens axis along the real axis of the complex plane. This process leads to a lengthy tenth-order polynomial in z, which can not be solved analytically.

One way to solve the lens equation and calculate the corresponding light curves of a triple-lens system is the inverse ray-shooting (IRS) method (Kayser et al. 1986; Wambsganss 1990, 1999), discussed in Appendix. One method to increase the performance speed of IRS method is using tree algorithm as explained in Sajadian & Rahvar (2010).

In the next subsection, we will review some degeneracies in the triple-lens equation.

2.2. Degeneracies in Triple Lens Equation

There are many parameters involved in the shapes of light curves for microlensing events and consequently, they can have different shapes. Sometimes, this can lead to a parameter degeneracy in the modeling of the event either accidentally (see, e.g., Gaudi 1998) or due to symmetry of the lens equation (see, e.g., Gould 1994).

In the case of triple microlensing, a four-fold degeneracy in the light curves can be found, which is similar to the case of close and wide degeneracy found in a binary lens (Song et al. 2014). Three important degeneracies are expected for triple-lens microlensing events (which are discussed in detail in Song et al. 2014.): discrete degeneracy, four-fold close/wide degeneracy, and continuous external shear degeneracy. Below, we briefly review each degeneracy.

Discrete degeneracy arises if one reverses the sign of the three parameters (u_0, α_0, ϕ), which is owing to the symmetry of the lens equation. This degeneracy can be resolved by measuring the second-order parallax effect. In planetary microlensing, where the mass ratios are $q_{21} \ll 1$ and $q_{31} \ll 1$, one can denote the planetary positions in complex notation (Equation (5)) as z_p. If one changes z_p into z_p^{-1}, the shape of the central caustics remains the same. This degeneracy can also be found in the case of binary lenses (Dominik 1999) and it is not just limited to triple lenses.

Finally, if one rewrites the triple-lens equation and expands the deflection terms caused by two of the masses (m_2 and m_3) at the location of the primary mass (m_1) using the Taylor expansion, we end up arriving at a lens equation similar to the case of binary lenses (Equation (2)). The important consequence of this continuous degeneracy is that in some cases, multiplanetary systems may be mistakenly detected as a single-planet system (Song et al. 2014).

2.3. Detection Probability of Triple Lensing Events

For detecting an exoplanet via microlensing, a signal is considered planetary if the deviations between the light curve calculated by the binary lens model (where one of the lens objects is planetary) and the simple single lens model is larger than a carefully chosen critical value. The Gould & Loeb criterion (Gould & Loeb 1992) provides a reliable criterion by considering deviations as planetary signals when a few observational points deviate consecutively from the single-lens light curve.

Ryu et al. (2011) show that if we consider the Gould & Loeb criterion for detecting a planet, for most cases, the detection probability of the low-mass planet in the triple-lens system is very similar to that in the binary lens system. The reason for this similarity is due to the lens superposition in the central regions (Han et al. 2001). It should also be noted that if the interference between caustics of the two planets change the original shapes, the binary superposition would not work well.

Additionally, it can be demonstrated that for the low-magnification events, where the source star only passes one of the planetary caustics, the probability of detecting the second planet is very low (Han & Park 2002). But, if the source star passes the main caustic (i.e., the high-magnification events), the probability of detecting the second planetary companion increases dramatically to unity (Griest & Safizadeh 1998). This is due to the closeness of planets to the Einstein radius and makes microlensing a unique method for detecting multi-planetary systems in such situations (Gaudi 2012).

3. Microlensing Magnification Map Analysis

Magnification maps are two-dimensional planes that show the magnification in the light of the source star in a region of the source plane. In a magnification map, each point is a solution of the lens equation (Equation (5)) regardless of the source trajectory. Therefore, magnification maps are helpful tools for discussing and analyzing microlensing events and their magnification.

In this section we analyze different configurations of the triple-lens magnification maps by evaluating the change in average magnification due to the second planet when the corresponding parameters of the system change and evolve.

The magnification due to lens objects from a point-like source star in any coordinate, x, of the source plane can be easily calculated by the inverse of the determinant of amplification matrix (Schneider et al. 1992):

$$\mu(\boldsymbol{x}) = \frac{1}{detA(\boldsymbol{x})}, \qquad (6)$$

where the amplification matrix is:

$$A(\boldsymbol{x}) = \mathbf{1} - \frac{\partial \boldsymbol{\alpha}(\boldsymbol{x})}{\partial \boldsymbol{x}}. \qquad (7)$$

If we input deflection angles due to binary (Equation (1)) and triple lenses (Equation (3)) in Equation (6) and consider the source plane as a $L_x \times L_y$ rectangular plane consisting of $N_x \times N_y$ points, i.e., pixels, we get triple-lens and binary lens magnification maps due to a point-like source star, respectively.

Furthermore, the average magnifications due to binary and triple lensing systems can be derived similarly as:

$$\langle \mu \rangle = \frac{1}{N_x \times N_y} \sum_{i}^{N_x} \sum_{j}^{N_y} \mu(x_{ij}). \qquad (8)$$

Now, the magnification due to the second planet can be defined as the deviation between the mean magnifications of triple, $\langle \mu_t \rangle$, and binary systems, $\langle \mu_b \rangle$,:

$$\mu_3 = \langle \mu_t \rangle - \langle \mu_b \rangle. \qquad (9)$$

There are some regions of the magnification map that the magnification is very high (almost infinite), i.e., the caustics (Erdl & Schneider 1993). Caustics can form due to the host star and the planets as well. Studying the properties of the planetary
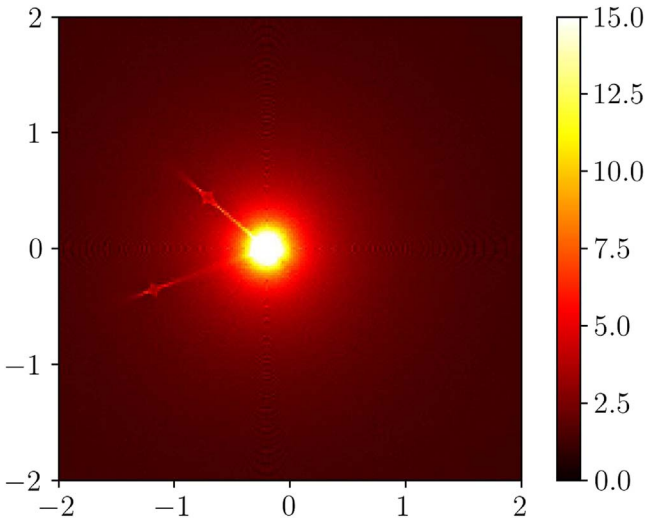
Figure 2. The orbital motion of two planets around the host star and the change in the system's magnification map. The color bar displays the mean magnification at each point in the source plane. An animated version of this figure is available. Its real-time duration is 16 s. The planetary caustics become relatively larger and fainter as they move closer to the host star in their respective orbits.

(An animation of this figure is available.)

caustics is important because the characteristics of the corresponding planetary signals in the microlensing light curve depend highly on them (Han 2006).

One of the most important properties of planetary caustics is their size or area, since it is used to determine the probability of detecting the planet. If the planetary caustic is big enough, there is a higher chance of a source star passing through, or close, to it. This in turn leads to a more detectable planetary signal.

It is known that a planet and its host star engage in a Keplerian motion, where they move in elliptic orbits around their common center of mass. This motion effects the magnifications due to each planet and the size of their caustics. However, if the xallarap effects can be neglected (Rota et al. 2021), a planetary signal in the microlensing light curve only represents a snapshot of the planet at its current angular separation from the host star, and does not depend on its orbital motion (Rahvar & Dominik 2009).

Figure 2 shows an animation of the change in the magnification map of a multiplanetary system which is caused by the orbital motions of two planets around the host star. It can be seen that the sizes of the planetary caustics change as the planets rotate around the barycenter. Additionally, the color of the caustics also changes, which represents the variation in the mean magnification of each caustic.

As it was mentioned in the introduction, the case of gravitational microlensing due to binary lenses has been studied extensively before. Also, In subsection 2.1, the main parameters of a triple-lens system were reviewed. Some of these parameters are only introduced in the case that the third lens (the secondary planet) exists. These parameters are: (q_{31}, s_{31}, ϕ).

In order to measure and discuss the changes in μ_3, we assume that the parameters of the primary planet are constant and only those of the second planet vary. The change in the ϕ angle was demonstrated in Figure 2.

In order to investigate the dependence and change of μ_3 with its angular separation s_{31} and mass ratio q_{31}, we consider the
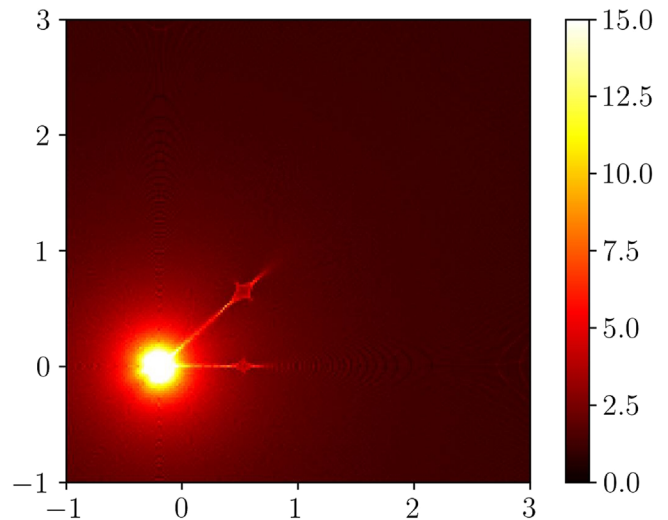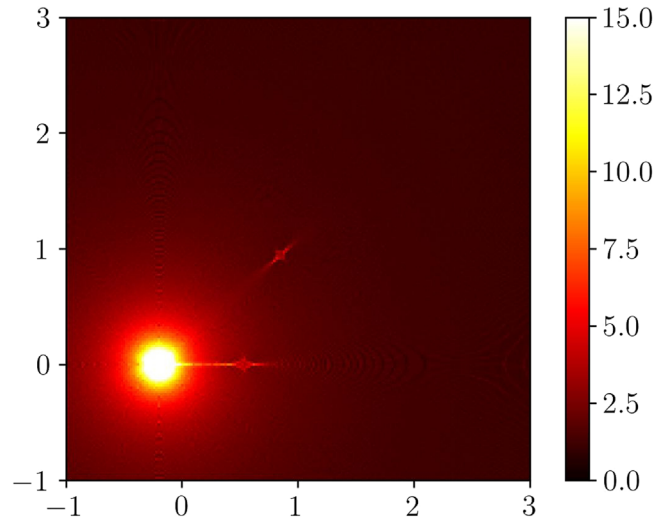

Figure 3. Top panel: this animation illustrates the dynamic change in the magnification map of the system as the separtion of the second planet from the host star (s_{31}) changes. The second planetary caustic becomes smaller and brighter as it moves away from the star. Bottom panel: this animation shows that dynamic change in the magnification map of the system as the mass ratio of the second planet (q_{31}) changes. The second planetary caustic becomes largers and brighter as the mass ratio increases. An animated version of this figure is available. Its real-time duration is 8 s.

(An animation of this figure is available.)

position of the first planet constant at $\theta = 0°.0$, $s_{21} = 1.0\,\theta_E$ with the mass ratio $q_{21} = 9 \times 10^{-4}$ (which is about the mass ratio of the planet Jupiter and Sun). The angle ϕ of the second planet is also considered constant at 60°.

First, we consider s_{31} varying between $0.9\,\theta_E$ and $2.5\,\theta_E$ where the second planet is also a Jovian planet with the mass ratio $q_{31} = 9 \times 10^{-4}$. The top panel of Figure 3 shows the dynamic change in magnification and area of the second planetary caustic with respect to its separation from the host star. We can see that the second planetary caustic becomes brighter (which represents the increase in its average magnification) and smaller as the second planet moves away from the star. The change in μ_3 with separation s_{31} and the best-fitted curve are shown in Figure 4(a). It can be seen that μ_3 increases with s_{31}. However, some deviations from the best-fit curve are visible in this figure, which are mostly caused by the approach and retreat of the second planet to the primary planet.
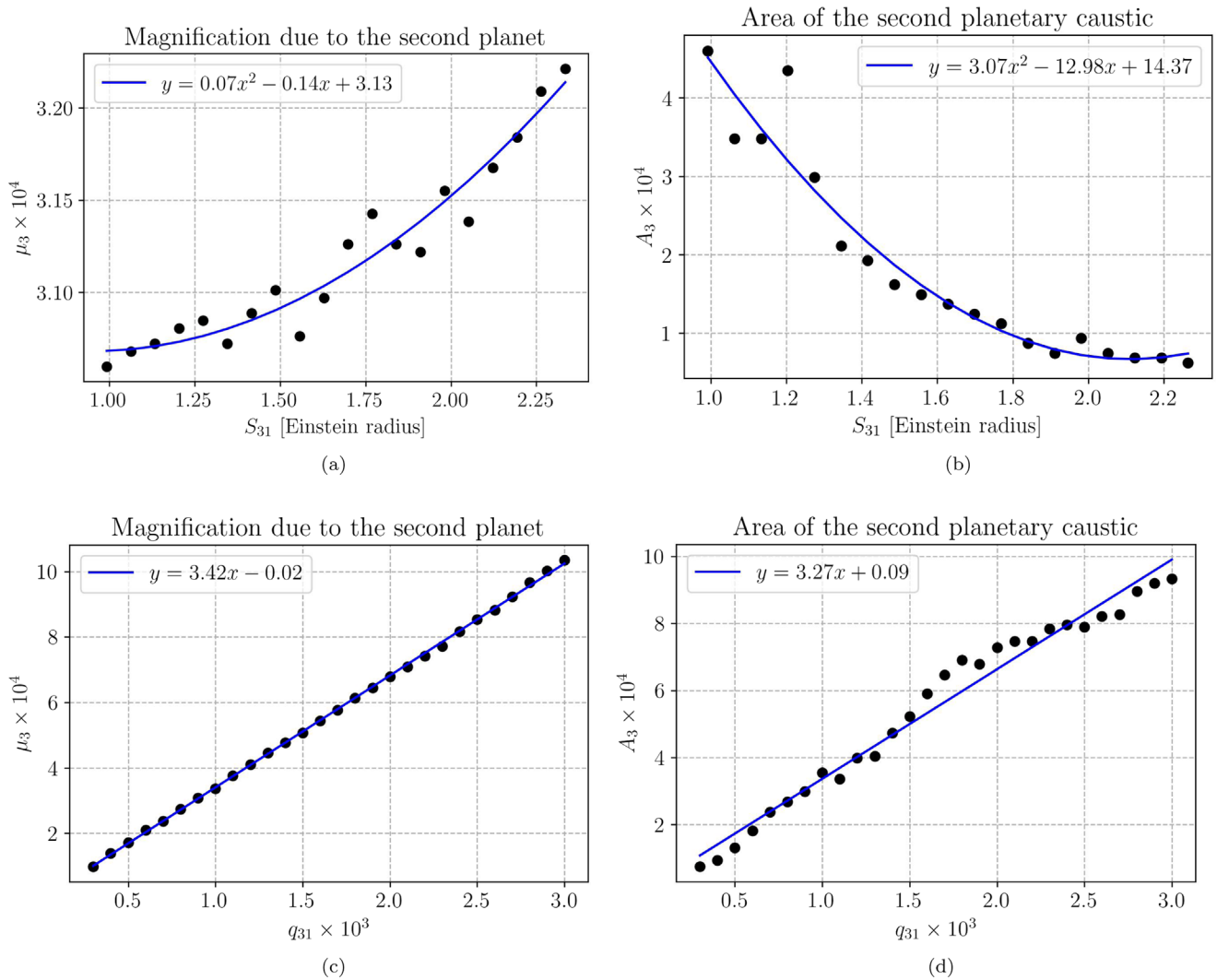
Figure 4. Panels (a) and (b) show the change in the mean magnification and caustic area of the second planet with respect to its separation (s_{31}). Figure (c) and (d) show the change in the mean magnification and caustic area of the second planet with respect to its mass ratio (q_{31}).

It should also be noted that, although the mean magnification increases with distance, but the area of the caustic decreases considerably, which is shown in Figure 4(b).

Then, we assume that the position of the second planet remains constant at $s_{31} = 1.1\,\theta_E$ and the mass ratio, q_{31} changes between 3×10^{-4} and 3×10^{-3}. The dynamic changes of the second planetary caustic are illustrated in the bottom panel of Figure 3. We can see that the second planetary caustic becomes brighter and larger (therefore, more detectable) as q_{31} increases. Figure 4(c) demonstrates the change in μ_3 as q_{31} increases. We can see that μ_3 increases linearly with the best-fit line: $y = 3.42x - 0.02$. The change in the area of this caustic is also shown in Figure 4(d), which shows that the caustic area (and the detection probability) of the second planet also increases linearly with respect to q_{31}.

4. The Roman Galactic Time Domain Survey

The Roman space telescope's Galactic Time Domain Survey (RGTDS) will detect an unprecedented number of exoplanets by monitoring the light curves of a large sample of stars toward the center of our galaxy. RGTDS is expected to discover bound exoplanets where the planets have distances in the range of 1 au and more from their host star using the gravitational

microlensing (Penny et al. 2019). Another possible discoveries by the Roman telescope are detection of habitable exoplanets, exomoons rotating free floating planets, and exoplanets around source stars (Bagheri et al. 2019; Sajadian 2021b; Sajadian & Sangtarash 2023).

In order to explore the detection of multiplanetary systems in RGTDS, we need to simulate a sample of different triple-lens planetary microlensing light curves and see if there is a significant difference between the triple and binary models that is observable by the Roman telescope.

We prepared a sample of 500 microlensing events where we considered both binary and triple systems and their difference. In the triple models, the planet that was considered in the corresponding binary systems also exists, with the addition of another planet. This way we can investigate that if a planet is detected with microlensing and the Roman telescope, are the effects of the second planet also detectable in the light curve.

For preparing our sample, we performed a Monte Carlo simulation by taking into account all of the relevant factors, e.g., mass ratios, angular separations, radius of the source star, impact parameter, photometric accuracy, etc. Also, instead of considering the position of the host star as the center of our reference frame, we make a rectangular plane with the size of
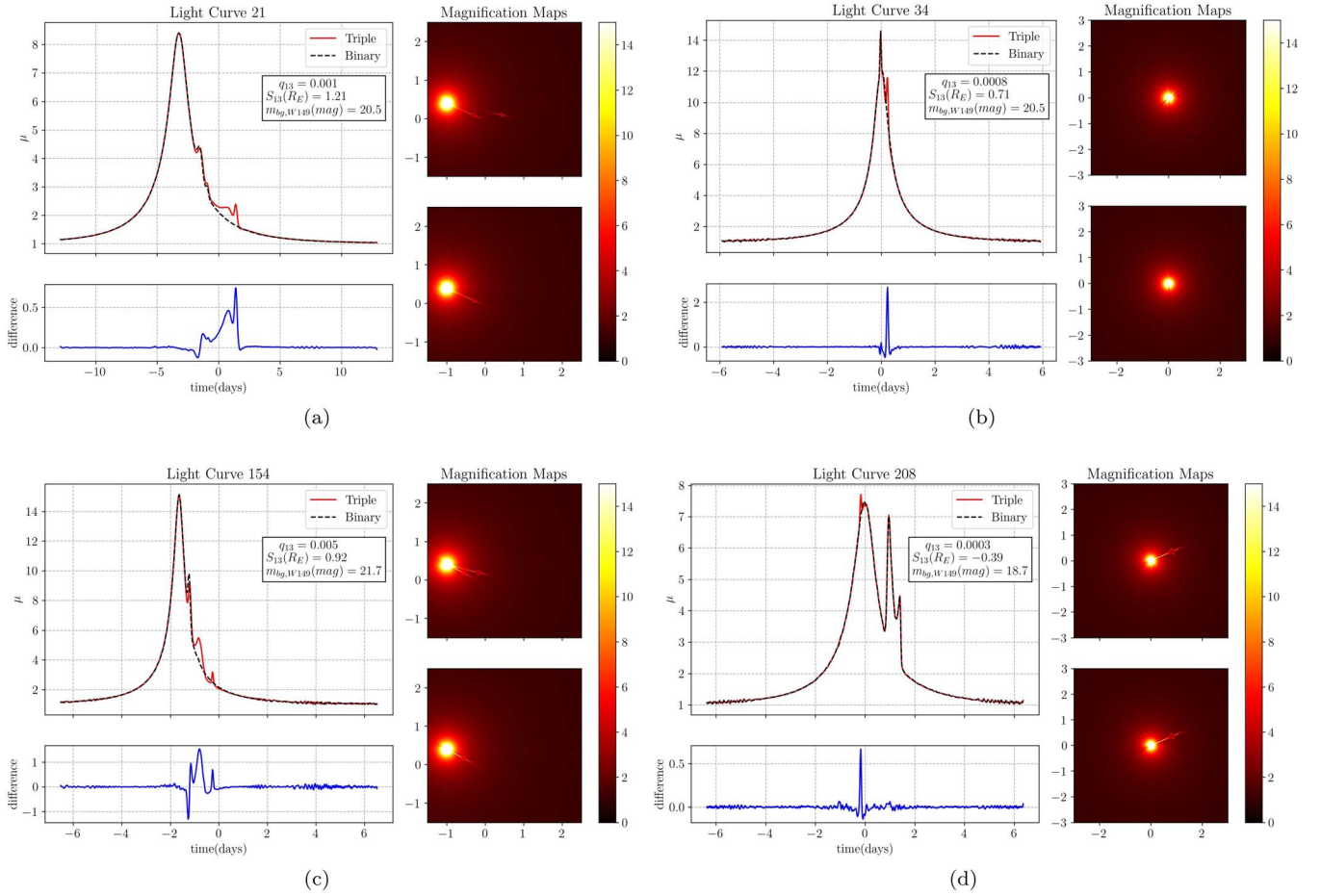
Figure 5. Light curves of four different microlensing events. In each figure the triple and binary models and their difference are illustrated. The magnification map on the top right of each light curve corresponds to the configurations of the lenses and the path of the souce star where there is a second planet (the red curve), whereas the maginfication map at the bottom represents the binary system configuration (the dashed black curve).

$L_x \times L_y$ around the path of the source star and consider the center of this plane as our reference frame. This approach makes the light-curve simulations (which are explained in Appendix) easier and allows for a wide range of samples by just moving the positions of the lens objects with respect to the origin.

Four light curves taken from the sample are shown in Figure 5. The light curves corresponding to triple systems are shown with the red curve, whereas the binary system light curves are illustrated with a dashed black curve. The difference between the triple and binary systems are displayed with a blue curve at the bottom of each light curve. We can see that the planetary signal due to the second planet is clearly visible in every light curve.

To simulate the synthetic data points taken by the Roman telescope, we assume these observations are done in the W149 Filter, which is a combination of the stellar magnitude in the standard bands as W149 $= (M_H + M_J + M_K)/3$, where M_H, M_J, and M_K are stellar absolute magnitudes in the standard filters H, J, and K, respectively. The photometric properties of stars in the simulation are determined using the Galactic Besançon model[1] (Robin et al. 2004, 2012). We use the 3D extinction map by Marshall et al. (2006), and the relation between extinctions in different filters given by Cardelli et al. (1989).

The Roman telescope can detect stars with the apparent magnitude in the range W149 $\in [14, 26]$ mag (Penny et al. 2019).

The cadence between data is fixed at 15.16 minutes. Roman will detect the Galactic bulge during six 62 days observing seasons.[2] Three seasons will be done during two first years of the Roman mission, and others will happen during two last years of its mission. So there is a long gap between first three observational seasons and others.

In fact, the Roman telescope can detect the Galactic bulge only during two 62 days time intervals in a year. Hence, the time interval between two observing seasons will be at least 120 days. More details about these simulations can be found in Sajadian (2021b).

As it was mentioned in Section 2.3, in planetary microlensing with one planet, the difference between the χ^2 values derived from fitting the real binary model, χ^2_{binary}, and the best-fitted single lens model, χ^2_{single} is considered for justifying a detection. Here, we consider the same notion for investigating that if a second planet is detected by Roman. We assume that the system is in fact triple and take the following value as our

---

[1] https://model.obs-besancon.fr/
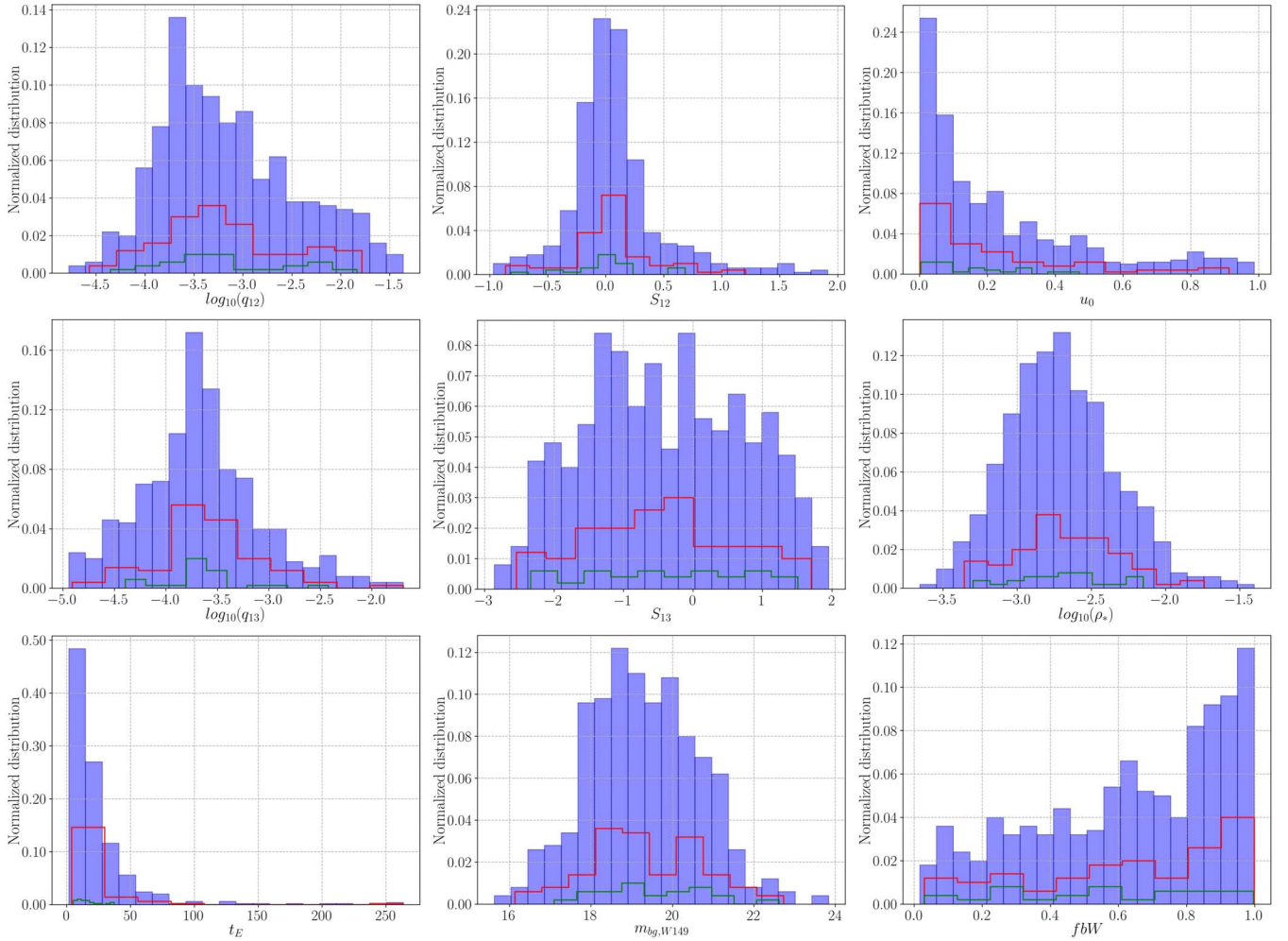
[2] Roman Galactic Bulge Time Domain Survey

Figure 6. Visualizations of statiscical distributions of the parameters used in the simulated data set and the results. The red curve shows the detected multiplanetary systems with low sensitivity and the green curve shows the ones with high sensitivity.

criterion for detecting the second planet:

$$\Delta\chi^2 = \chi^2_{\mathrm{triple}} - \chi^2_{\mathrm{binary}}. \quad (10)$$

We have calculated the $\Delta\chi^2_n$ (normalized $\Delta\chi^2$) values for our sample of light curves by considering various apparent magnitudes at the baseline W149 (m_{W149}), different Einstein crossing times (t_{E} [days]), planetary mass ratios (q_{12} and q_{13}), angular separations (s_{12} and $s13$), etc.

The threshold of $\Delta\chi^2_n > 100$ is usually considered as criterion for detecting a planetary signal with weak sensitivity in the light curve of a microlensing event. Whereas, the threshold of $\Delta\chi^2_n > 500$ indicates a planetary signal detection with high sensitivity. If we consider these criteria for our light-curve sample, 85 out of 500 events convey a second planetary signal detected by Roman, including 24 events where the second planetary signal was robust. This gives an efficiency between 4.8% and 17%.

The statistical distribution of our simulated parameters are shown in Figure 6. The red curve shows the detected multiplanetary systems with low sensitivity and the green curve shows the ones with high sensitivity.

It is also worth noting that since Roman will provide a very large sample of microlensing events with planetary signals, even the high sensitivity criterion (which has an efficiency of 4.8%) would result in the detection of an unprecedented number of multiplanetary systems via gravitational microlensing.

The light-curve data and the full simulation results (including the photometric simulations) of the Roman space telescope can be found in Fatheddin (2023).

5. Conclusions

It is quite plausible that a star can host multiple planets, as it has been evident in the transit data from space telescope like Kepler and the Transiting Exoplanet Survey Satellite.

In this work, we studied the detection and characterization of multiplanetary systems with gravitational microlensing. We have shown that different parameters can affect the shape of microlensing magnification maps and proportionately change the shape of corresponding light curves. Also, we have shown that the area of the second planetary caustic, and therefore its detection probability, is also highly dependent on its configurations (i.e., its separation from the host star or its mass ratio).

We performed Monte Carlo simulations for all of the parameters involved in triple-lens planetary events and simulated 500 light curves based on the results. We studied the possibility of detecting these multiplanetary systems with the future implementation of the Roman space telescope. Our results show that Roman will have a detection efficiency between 4.8% and 17%, which will lead to a large and diverse

sample of multiplanetary systems using the microlensing method.

In this paper, we mainly considered the multiplanetary system consisting of a host star with two planets. However, this results can also be simply investigated for a system with a higher number of planets.

Acknowledgments

Appendix
Magnification Map and Light-curve Simulations

Most of the simulations of binary microlensing events are modeled by using the contour integration method, which is based on the Green's theorem (Gould & Gaucherel 1997; Dominik 1998; Bozza et al. 2018) in order to infer the characteristics and the physical parameters of the events. In this method, the total area of the lensed images is calculated, which leads to the magnification factors and light curves. Inverse ray shooting (IRS; Kayser et al. 1986; Wambsganss 1990, 1999) is not used in these cases due to its inefficiency for fitting light curves of low-multiplicity point mass lenses of microlensing planetary systems (see Rhie 2002). But, IRS proposes an efficient method for modeling planetary microlensing events with more than two lenses (Bennett 2010). Here, we briefly explain the IRS method which was used for simulating the magnification maps of Section 3 and light curves of Section 4. This algorithm is based on our discussion in Sections 1 and 2.

When we observe a Gravitational Lensing or Microlensing event, the light rays are emitted from the source (which is in the source plane) and after moving through the Lens plane, they are deflected due to the gravitational field of the Lens. The special theory of relativity states that the light rays are "time-invariant," which means that the time reverse of the path that light rays take from any source to an observer is allowed. This is the main notion behind IRS.

In the formalism of IRS, for inverting the lens equation, Equation (5) (i.e., knowing the position, distortion, magnification, of the image(s) of the source), we shoot rays backwards from the observer to the lens plane and by calculating the deflection angle of each ray (Equation (3)), we find the location of where the light ray hits the source plane, and therefore forming an image there. Because of the very long distances in astronomy, the observer can not differentiate between most close and far objects; so, in IRS, everything is happening in one plane, which is the observed plane.

Since the source is moving behind the Lens objects (we usually take the lens to be stationary), we can make a set of frames and in each frame propagate the rays by simulating the motion of the source and then take a snapshot. Finally a dynamic light curve can be made by calculating the areas of the formed images and then dividing them by the area of the unlensed source.

We also note that in our simulations, in order to consider the finite source effects, we have considered the source star as an array-like homogeneous disk with the radius ρ_*.

ORCID iDs

Hossein Fatheddin https://orcid.org/0000-0002-7611-9249
Sedighe Sajadian https://orcid.org/0000-0002-2859-1071

References

Alcock, C., Akerlof, C. W., Allsman, R. A., et al. 1993, Natur, 365, 621
Alcock, C., Allsman, R. A., Alves, D., et al. 1997, ApJ, 486, 697
Alcock, C., Allsman, R. A., Alves, D. R., et al. 2000, ApJ, 542, 281
Aubourg, E., Bareyre, P., Bréhin, S., et al. 1993, Natur, 365, 623
Bagheri, F., Sajadian, S., & Rahvar, S. 2019, MNRAS, 490, 1581
Bennett, D. P. 2008, in Exoplanets, ed. J. W. Mason (Berlin: Springer), 47
Bennett, D. P. 2010, ApJ, 716, 1408
Bennett, D. P., & Rhie, S. H. 1996, ApJ, 472, 660
Bennett, D. P., Udalski, A., Bond, I. A., et al. 2020, AJ, 160, 72
Bozza, V., Bachelet, E., Bartolić, F., et al. 2018, MNRAS, 479, 5157
Cardelli, J. A., Clayton, G. C., & Mathis, J. S. 1989, ApJ, 345, 245
Dominik, M. 1998, A&A, 333, L79
Dominik, M. 1999, A&A, 349, 108
Dyson, F. W., Eddington, A. S., & Davidson, C. 1920, RSPTA, 220, 291
Erdl, H., & Schneider, P. 1993, A&A, 268, 453
Fatheddin, H. 2023, Roman-Multi-Planetary-data, 1.0,, Zenodo, doi:10.5281/zenodo.8075195
Fatheddin, H., & Sajadian, S. 2022, MNRAS, 514, 4379
Fischer, D. A., Howard, A. W., Laughlin, G. P., et al. 2014, in Protostars and Planets VI, ed. H. Beuther et al. (Tucson, AZ: Univ. of Arizona Press), 715
Gaudi, B. S. 1998, ApJ, 506, 533
Gaudi, B. S. 2012, ARA&A, 50, 411
Gaudi, B. S., Bennett, D. P., Udalski, A., et al. 2008, Sci, 319, 927
Gould, A. 1994, ApJL, 421, L75
Gould, A., & Gaucherel, C. 1997, ApJ, 477, 580
Gould, A., & Loeb, A. 1992, ApJ, 396, 104
Griest, K., & Safizadeh, N. 1998, ApJ, 500, 37
Han, C. 2006, ApJ, 638, 1080
Han, C., Chang, H.-Y., An, J. H., & Chang, K. 2001, MNRAS, 328, 986
Han, C., & Park, M.-G. 2002, JKAS, 35, 35
Kayser, R., Refsdal, S., & Stabell, R. 1986, A&A, 166, 36
Kim, S.-L., Lee, C.-U., Park, B.-G., et al. 2016, JKAS, 49, 37
Liebes, S. 1964, PhRv, 133, 835
Livingston, J. H., Dai, F., Hirano, T., et al. 2019, MNRAS, 484, 8
Maltagliati, L. 2019, NatAs, 3, 1049
Mao, S., & Paczynski, B. 1991, ApJL, 374, L37
Marshall, D. J., Robin, A. C., Reylé, C., Schultheis, M., & Picaud, S. 2006, A&A, 453, 635
Mayor, M., & Queloz, D. 1995, Natur, 378, 355
Penny, M. T., Gaudi, B. S., Kerins, E., et al. 2019, ApJS, 241, 3
Rahvar, S., & Dominik, M. 2009, MNRAS, 392, 1193
Refsdal, S. 1964, MNRAS, 128, 295
Refsdal, S. 1966, MNRAS, 134, 315
Rhie, S. H. 2002, arXiv:astro-ph/0202294
Robin, A. C., Marshall, D. J., Schultheis, M., & Reylé, C. 2012, A&A, 538, A106
Robin, A. C., Reylé, C., Derrière, S., & Picaud, S. 2004, A&A, 416, 157
Rota, P., Hirao, Y., Bozza, V., et al. 2021, AJ, 162, 59
Ryu, Y.-H., Chang, H.-Y., & Park, M.-G. 2011, MNRAS, 412, 503
Sahu, K. C., Anderson, J., Casertano, S., et al. 2022, ApJ, 933, 83
Sajadian, S. 2021a, MNRAS, 506, 3615
Sajadian, S. 2021b, MNRAS, 508, 5991
Sajadian, S., & Rahvar, S. 2010, MNRAS, 407, 373
Sajadian, S., & Sahu, K. C. 2023, AJ, 165, 96
Sajadian, S., & Sangtarash, P. 2023, MNRAS, 520, 5613
Sako, T., Sekiguchi, T., Sasaki, M., et al. 2008, ExA, 22, 51
Schneider, P., Ehlers, J., & Falco, E. E. 1992, Gravitational Lenses (Berlin: Springer)
Schneider, P., & Weiss, A. 1986, A&A, 164, 237
Song, Y.-Y., Mao, S., & An, J. H. 2014, MNRAS, 437, 4006
Sumi, T. 2014, AAS Meeting Abstracts, 224, 210.05
Udalski, A., Szymanski, M., Kaluzny, J., et al. 1993, AcA, 43, 289
Udalski, A., Szymański, M. K., & Szymański, G. 2015, AcA, 65, 1
Wambsganss, J. 1990, PhD thesis, Ludwig Maximilians University
Wambsganss, J. 1999, JCoAM, 109, 353
Witt, H. J. 1990, A&A, 236, 311
Witt, H. J., & Mao, S. 1995, ApJL, 447, L105

Wright, J. T., & Gaudi, B. S. 2013, in Planets, Stars and Stellar Systems. Volume 3: Solar and Stellar Planetary Systems, ed. T. D. Oswalt, L. M. French, & P. Kalas (Dordrecht: Springer), 489